# Revealing In-plane Movement of Platinum in PEFCs after Heavy-duty Vehicle Lifetime

Kaustubh Khedekar[1,2], Andrea Zaffora[3,4], Monica Santamaria[4], Matthew Coats[5], Svitlana Pylypenko[5], Jonathan Braaten[6], Plamen Atanassov[3], Nobumichi Tamura[7], Lei Cheng[6‡], Christina Johnston[6‡], Iryna V. Zenyuk[1,2,3‡]

[1]Department of Materials Science & Engineering, University of California Irvine, Irvine, CA 92617

[2]National Fuel Cell Research Center, University of California Irvine, Irvine, CA 92617

[3]Department of Chemical & Biomolecular Engineering, University of California Irvine, Irvine, CA 92617

[4]Dipartimento di Ingegneria, University of Palermo, Palermo, Italy 90133

[5]Department of Chemistry, Colorado School of Mines, Golden, CO 80401

[6]Bosch Research and Technology Center North America, Sunnyvale, CA 94085

[7]Advanced Light Source, Lawrence Berkeley National Laboratory, CA 94706

‡Corresponding authors: Iryna.Zenyuk@uci.edu, Lei.Cheng2@us.bosch.com, Christina.Johnston@us.bosch.com.

## Abstract

Fuel cell heavy-duty vehicles (HDVs) require increased durability of oxygen reduction reaction electrocatalysts making knowledge of realistic degradation mechanisms critical. Here, identical location μ-X-ray fluorescence spectroscopy was performed on membrane electrode assemblies (MEAs). The results exposed heavy in-plane movement of electrocatalyst after HDV lifetime, suggesting that electrochemical Ostwald ripening may not be a local effect. Development of local loading hotspots and a preferential movement of electrocatalyst away from cathode catalyst layer cracks was observed. Heterogeneous degradation showed by a modified cathode gas diffusion layer MEA after HDV lifetime was successfully quantified thanks to the identical location approach. Further synchrotron μ-X-ray diffraction and fluorescence experiments were performed to obtain currently unknown correlation between electrocatalyst nanoparticle size increase and loading change. A direct correlation was discovered which developed only after HDV lifetime. The work provides direction to engineer immediate system-level mitigation strategies and to develop structured cathode catalyst layers with durable electrocatalysts.

To achieve zero carbon emissions, governments and industries across the world are implementing the use of clean hydrogen, targeting difficult to decarbonize sectors such as heavy-duty transportation, aviation, shipping and chemical manufacturing. Heavy-duty vehicles (HDVs) make up only 7 % of the total vehicles on-road[1] but produce nearly 26 % of the United States (US) transportation sector greenhouse gas emissions[2]. Polymer electrolyte fuel cells (PEFCs) are an excellent candidate to power emission free HDVs particularly due to their ability to increase driving range at a much smaller additional weight penalty. However, initial system cost remains a significant challenge for large scale adoption mainly due to the use of platinum-group metal (PGM) electrocatalysts to promote oxygen reduction reaction (ORR). For a projected manufacturing volume of 100,000 systems/year, the calculated PEFC stack cost is $41.93/kW of which 53% is contributed by electrocatalyst and applications[3]. Current approach to reduce initial cost and improve performance by

utilizing highly dispersed PGM nanoparticles (2-3 nm) on carbon support adversely affects stack lifetime[4–6]. Small well-dispersed nanoparticles result in improved PGM utilization by effectively increasing the electrochemically active surface area (ECSA). This boosts power density while reducing PGM loading and cost/kW. However, repeated oxidation-reduction of platinum (Pt) nanoparticles during HDV lifetime causes Pt dissolution in the cathode catalyst layer[4,6]. This dissolution leads to loss in the ECSA via deposition of Pt in the membrane and increase in Pt nanoparticle size through electrochemical Ostwald ripening and/or coalescence[6,7]. In addition, nanoparticles of Pt alloyed with transition metals such as cobalt (Co) and nickel (Ni) to reduce cost while enhancing ORR activity face significant leaching of transition metals within the voltage-pH range of PEFC operation[8]. Such transition metal leaching negates achieved improvement in ORR activity at the beginning of life. It also affects proton conduction and oxygen transport properties of ionomer causing loss in high current density performance[9]. The complex balance between cost, performance and durability of PEFCs coupled with the 2050 projection of 54% increase in HDV miles travelled[10] makes understanding electrocatalyst degradation a top priority to develop durable ORR electrocatalysts.

Recently, *in situ* identical location transmission electron microscopy (IL-TEM) and *ex situ* identical location scanning transmission electron microscopy (IL-STEM) techniques using aqueous electrolyte rotating disk electrode (RDE) setup have been utilized to elucidate electrocatalyst degradation mechanisms[11,12]. The more common IL-STEM uses a gold coated TEM grid which allows atomic level imaging, energy dispersive X-ray spectroscopy (EDS) and electron energy-loss spectroscopy (EELS) analysis of electrocatalyst in the same region at different lifetime stages. Results from above discussed techniques combined with flow cell inductively coupled plasma mass spectroscopy (ICP-MS) have identified Pt dissolution as the primary and dominant degradation mechanism followed by Pt nanoparticle size increase through migration-coalescence and Pt nanoparticle detachment from carbon support. Contrarily, membrane electrode assembly (MEA) tests have shown that nanoparticle size increase by electrochemical Ostwald ripening is the dominant degradation mechanism[13]. Such disparity is caused by the complicated cathode catalyst layer operation environment within MEA, where multiple transport processes at the electrocatalyst-support-ionomer interface play a crucial role[14]. In addition to electrocatalyst and ionomer properties, the transport processes are also affected by the operating conditions, PEFC components and cathode catalyst layer morphology[15,16]. This is also the reason for poor translation of electrocatalyst ORR activity from RDE to MEA-scale[14]. Furthermore, electrocatalyst degradation is strongly influenced by loading, and RDE working electrodes employ ultra-low electrocatalyst loading deposited on either carbon or gold surface compared to MEA-scale where a much higher loading is deposited on membrane resulting in a 100x loading difference. This can lead to degradation rates that deviate substantially from realistic conditions. Various studies have attempted to eliminate this disparity by using different electrolyte flowrates, operating temperatures and electrode configurations in the RDE setup[12,17]. However, concerns regarding the relevance of identified RDE-scale degradation mechanisms to MEA-scale remain[14]. To date, MEA-scale AST studies commonly rely on *ex situ* TEM of scraped electrocatalyst from the cathode catalyst layer and SEM/EDS analysis of MEA cross-sections[7,13]. Although, this reveals nanoparticle size increase and through-plane changes like Pt band formation, the techniques fail to capture in-plane degradation phenomenon. Recently synchrotron μ-X-ray diffraction studies revealed important in-plane heterogeneity in Pt nanoparticle size increase due to influence of operating conditions and PEFC components[18,19]. Thus, to mitigate the risk of misidentifying degradation mechanisms and misdirecting the electrocatalyst material development it is very important to validate the results with thorough MEA-scale analysis which captures realistic aspects of electrocatalyst degradation.

Here, commercially available catalyst coated membranes (CCMs) designed for potential HDV application were subjected to accelerated stress tests (ASTs) simulating HDV lifetime. A simple method was utilized to achieve MEA-scale identical location μ-X-ray fluorescence (IL-μ-XRF) spectroscopy maps before and after the AST. From the total three-dimensional movement, IL-μ-XRF mapping of the MEAs performed near the inlet and outlet regions of cathode gas flow field captured the two-dimensional in-plane movement

of Pt electrocatalyst. Analysis of identical locations revealed distinct changes in Pt loading strongly influenced by its initial distribution and by cathode catalyst layer morphology. A modified cathode gas diffusion layer (GDL) MEA was used to highlight the effect of PEFC components on electrocatalyst degradation. The resulting heterogeneous Pt degradation was successfully quantified using the developed method. Finally, synchrotron μ-X-ray diffraction (μ-XRD) and μ-XRF experiments were performed successively on identical locations to establish a currently unknown correlation between nanoparticle size increase and changes in loading after the AST. Electrochemical characterization was performed at various stages of the AST to support the spectroscopic analysis.

**Simulating HDV lifetime**

Using a representative HDV drive cycle for Class 8 truck reported by the California Air Resource Board, the National Renewable Energy Laboratory simulated the cell voltages for a hybrid 250 kW fuel cell system/35 kWh battery traction power system with a minimum idle power of 20 kW to limit the upper potential limit (UPL) at 0.9 V[20,21]. Electrocatalyst degradation is severely impacted by high UPLs, thus UPL for HDV lifetime needs to be clipped at 0.9 V to ensure that US Department of Energy (DOE) interim and ultimate system lifetime targets of 25,000 and 30,000 hours are reached[22]. A further low value of UPL cannot be used as it decreases overall system efficiency while causing thermal management issues. Based on the simulated cell voltages and previous DOE recommended light-duty vehicle (LDV) AST equating to ≥ 5000 hours of system lifetime[22], a square cell voltage cycle as depicted in **Figure 1a** with lower potential limit (LPL) of 0.6 V and UPL of 0.9 V with a hold time of 3 seconds each was adopted in this study. To equate the AST to ≥ 25,000 hours of HDV lifetime, the 6 second square cell voltage cycle was repeated for 90,000 times in a non-reactive cathode gas ($N_2$) environment at 80°C in 100% relative humidity (RH) under atmospheric pressure, giving a total AST time of 150 hours (Methods). Although, real-world HDV operation is in a reactive cathode gas environment (air) at wide range of temperatures and in varying RH, the $N_2$ environment AST was selected particularly to focus on electrocatalyst degradation. Detailed and extensive benchmarking of this AST reported in the literature ensures that mechanistic conclusions drawn in this study and their implications on real-world HDV operation are highly relevant. It is also crucial to mention that several efforts primarily led by the Million Mile Fuel Cell Truck consortium (M2FCT) are ongoing to meet the urgent need of ASTs better adapted for HDV applications.

**Fundamentals of Pt degradation**

The standard Nernst equilibrium potential of direct dissolution reaction of Pt ions when corrected for the increased surface energy of nanoparticles can decrease to ~ 0.5 V (1 nm and $10^{-6}$ M of $Pt^{2+}$) compared to ~ 1 V of bulk Pt. This is commonly known as the Kelvin or Gibbs-Thompson effect[4]. This effect can also be observed for dissolution of Pt ions during reduction reaction of Pt oxide. The equilibrium potential for dissolution of Pt ions from nanoparticles is further lowered by decreasing concentration of Pt ions[4]. Thus, purely based on thermodynamic analysis, significant degradation of Pt nanoparticles occurs via Pt dissolution within PEFC operational voltage (0.6 V to 1 V) and pH (~ 1 to 4) range. This also means that degradation is affected not only by electrocatalyst properties such as nanoparticle size[23], distribution[23,24], crystalline orientation, dispersion and carbon support type but also by the local cathode catalyst layer environment[25]. The local environment can be affected by operating conditions like cell temperature, RH, reactant flow rates and by PEFC components like micro-porous layer (MPL) of GDL and flow field. Cell temperature and RH are serious Pt degradation stressors which can be influenced in the local environment by cathode catalyst layer morphology. These include but are not limited to features like porosity, in-plane/through-plane Pt loading distribution and catalyst layer cracks[26]. Liquid water flux in the cathode catalyst layer, affected by the interplay between operating conditions, PEFC components and morphology also plays crucial role to control local RH and Pt ion concentration consequently influencing electrocatalyst degradation[12,16].

Besides the ECSA loss due to migration-coalescence, dissolution of Pt ions results in three additional ECSA loss pathways as shown in **Figure 1b** where firstly, the Pt ions can reduce on nearby larger nanoparticles with lower surface energy. The Pt ions can also diffuse towards anode and get reduced in the membrane by crossover hydrogen to form a Pt band[5,7]. Physical location of such Pt band is governed by the partial pressures of hydrogen and oxygen during the AST[27]. For a non-reactive cathode gas ($N_2$) environment, Pt band is located near the membrane-cathode interface. And lastly, Pt ions can completely leave the system with effluent water. This ECSA loss pathway is less explored although ICP-MS reports of effluent water have detected concentration of Pt ions[12]. The dominant ECSA loss pathway of course depends on the thermodynamics of Pt dissolution, but it also depends heavily on the convoluted interplay between kinetics of Pt oxidation, dissolution and reduction[28]. As a result, the effects of UPL, LPL and time spent at each potential limit during the AST emerge. Electrochemical analysis of MEA tests coupled with *in situ* ICP-MS studies suggest that the cathodic step of AST cell voltage cycle (i.e. stepping from UPL to LPL) causes maximum dissolution of Pt ions followed by direct dissolution during the anodic step [28]. The cathodic dissolution is attributed to reduction of Pt oxide (~ 0.8 V) formed at the UPL. The formation rate and coverage of Pt oxide is greatly affected by the UPL and the hold time [4,28,29], respectively. Therefore, a higher value of UPL with longer hold time will result in increased Pt oxide formation and consequently higher dissolution during the cathodic step. Dissolution during the cathodic step also makes Pt degradation a function of number of AST cycles[29]. The rate of reduction of Pt ions is reported to be relatively high ≤ ~ 0.6 V [30]. Thus, a higher value of LPL also affects the amount of Pt oxide formed at UPL during the next cell voltage cycle as less clean Pt surface is available for oxide formation. For Pt-alloy catalysts, both the time spent, and value of LPL is of higher importance since reduction potential of the base metal is involved[31]. Ratio of Pt dissolution during the anodic vs cathodic step is a strong function of the UPL. Anodic step dissolution is important for low UPLs, cathodic step dissolution for high UPLs and dissolution during both steps for intermediate UPLs [4, 28]. Several studies are still ongoing to fully understand the effects of above discussed properties, conditions and parameters on electrocatalyst degradation.

**Electrochemical characterization**

Polarization curves with high frequency resistance (HFR) collected at 80°C in 100% RH under 150 kPa of absolute pressure in $H_2$-air (anode-cathode) differential conditions during various stages of the AST are plotted in **Figure 2a**. Except a very small drop within first 10,000 AST cycles, the cell HFR remains unchanged throughout the AST. Such slight initial decrease in HFR has been previously reported[15] and is usually attributed to additional cell conditioning. As the AST progresses and the electrocatalyst undergoes degradation, a monotonic increase in kinetic and mass transport cell overpotentials can be observed. An overpotential increase of ~ 25 mV and ~ 33 mV is seen at geometric current densities of 0.8 $A.cm^{-2}$ and 1.5 $A.cm^{-2}$ respectively. Thus, the MEA achieved set DOE target of ≤ 30 mV[32] of increase in overpotential at 0.8 $A.cm^{-2}$. A small change in the slope of polarization curves can be noticed between 60,000 and 90,000 AST cycles. As the HFR is constant, this change in slope could be due to increase in oxygen mass transport resistance usually caused by the decrease of Pt roughness factor (rf) below a threshold value[33]. **Figure 2b** shows ECSA (calculated by integrating the hydrogen underpotential deposition region from cyclic voltammograms in Supplementary Figure 1) plotted at different stages of the AST. The ECSA decreased by ~ 32% after 90,000 AST cycles. The loss in ECSA agrees well with the observed increase in cell overpotentials. Tafel plots generated from data collected in operating conditions same as the polarization curves but in $O_2$ cathode environment are plotted in **Figure 2c.** The ORR Tafel slope is close to literature reported value of 70 $mV.dec^{-1}$ in MEAs[34-36] and does not change through the AST. Plot inset **Figure 2c** shows the mass activity at 0.9 V calculated from the Tafel plots. A ~ 45% decrease is observed in mass activity which follows a loss trend similar to the ECSA.

**Identical location μ-X-ray fluorescence spectroscopy**

Using a thin polytetrafluoroethylene (PTFE) template with alignment markers (Methods), IL-μ-XRF spectroscopy was performed on MEA before and after HDV lifetime. The spectroscopy was performed in-plane on an area of 2048 μm by 2048 μm with a resolution of 2 μm by 2 μm near inlet and outlet of the serpentine cathode flow field. **Figure 3a** and **b** show the 2D IL-μ-XRF maps near inlet and outlet respectively. Corresponding loading histograms are shown in **Figure 3c** and **d**. Marked locations A,B,C in the inlet map before AST and A',B',C' after AST establish successful mapping of identical locations. Only one location is marked hereafter to signify identical location. A total average Pt loading of 559 ± 11 $\mu g.cm^{-2}$ was quantified in the before AST inlet map with presence of several local hotspots within initial distribution of Pt loading. The size of such local loading hotspots may differ, but it is a recurring feature found in various commercially available and in-house made CCMs fabricated using completely different techniques. One reason for development of such local loading hotspots is attributed to agglomeration of the carbon support influenced by solvent ratios, ionomer, drying conditions and dispersion methodology[37]. The before AST outlet map also shows features similar to the before AST inlet map with a total average Pt loading of 553 ± 11 $\mu g.cm^{-2}$ which falls within the observed spatial variation of ± 2% (Methods). The after AST inlet and outlet maps show a total average Pt loading of 551 ± 11 $\mu g.cm^{-2}$ and 548 ± 11 $\mu g.cm^{-2}$ respectively. A clear increase in the intensity of local loading hotspots and development of cracks can be noticed in both the inlet and outlet after AST maps. However, a higher degree of cracking can be observed in the outlet map suggesting some heterogeneous degradation between inlet and outlet. The loading histograms of inlet and outlet before AST show a unimodal initial distribution of Pt loading. The distribution stays unimodal after the AST with a negligible change in the total average Pt loading as it falls within the observed spatial variation. A larger representative area of ~ 4 $cm^2$ out of the 5 $cm^2$ active area was also mapped with a resolution of 20 μm by 20 μm (Supplementary Figure 2a). A total average Pt loading of 559 ± 11 $\mu g.cm^{-2}$ and 550 ± 11 $\mu g.cm^{-2}$ was quantified for the 4 $cm^2$ before and after AST maps respectively.

To study the increase in intensity of local loading hotspots, above IL-μ-XRF maps were closely examined before and after the AST. **Figure 4a** shows one of the many (Supplementary Figure 3) local 400 μm by 400 μm areas from inlet which delineates development of such local hotspots after AST. Marked locations A and A' in **Figure 4a** clearly indicate in-plane movement of Pt which led to evolution of a hotspot where the average total Pt loading increased from ~ 750 $\mu g.cm^{-2}$ to ~ 1100 $\mu g.cm^{-2}$. An average increase of ~ 32 % can be seen for formation of hotspots specifically observed in **Figure 4a.** Such hotspots evolved selectively in locations with local loading already ≥ 750 $\mu g.cm^{-2}$ confirming that initial Pt loading distribution plays a crucial role in how the Pt distribution will evolve during AST. Thus, formation of such hotspots could be driven by relatively low inter-nanoparticle distance in the initial stages and later by the (resulting) larger Pt nanoparticle sizes. The striking in-plane movement of Pt on the scale of tens of μm after AST may signify that electrochemical Ostwald ripening in the cathode catalyst layer is not a local effect as currently believed. **Figure 4b** shows another local 400 μm by 400 μm area before and after AST from the outlet. Such maps also revealed a preferential movement of Pt away from the cracks making them more prominent after AST. The preferential movement of Pt could be thermodynamically driven between the regions. The transmission images (Supplementary Figure 4) showed that cracks are present before AST and become more prominent after AST. Most likely, the cracks formed during the drying step of CCM fabrication and caused sparse distribution of Pt loading within. Different studies have reported that cracks result in low breakthrough pressure for removal of liquid water[38]. This can cause high liquid water flux in the cathode catalyst layer cracks consequently decreasing the local concentration of Pt ions. The sparse loading distribution within cracks coupled with low local Pt ion concentration can intensify Pt degradation in and around cracks[39,40]. The heavy in-plane movement of Pt along with the presence of loading hotspots within ~ 0 to 5 μm of a crack certainly substantiates the role of cathode catalyst layer morphology on Pt degradation. Cracks can also aid the through-plane movement of Pt ions either towards the membrane (via ionomer phase) or out of the cathode catalyst layer (via effluent water).

To understand if Pt degradation can be impacted by MEA components and to confirm if the developed identical location method could quantify such effects, a GDL with modified MPL was used on the cathode

of MEA subjected to HDV lifetime. Cracks of width ~ 30-50 μm were milled in the MPL (Methods) with a pitch of 1 mm in a direction perpendicular to the land/channels of the flow field and were confirmed by μ-X-ray computed tomography (Supplementary Figure 5). **Figure 5a** and **b** show IL-μ-XRF maps of inlet and outlet (before and after AST) respectively. Like the standard MEA, significant changes in Pt loading can be observed between maps before and after AST of both inlet and outlet regions of the modified MEA. However, in contrast to the standard MEA a substantial heterogeneous degradation after AST was noted between the inlet and outlet most likely due to poor thermal and water management of the modified GDL. A loss in the total average Pt loading of inlet from 545 ± 11 $\mu g.cm^{-2}$ to 477 ± 10 $\mu g.cm^{-2}$ was effectively quantified before and after AST. This ~ 13% loss in the total average Pt loading is significantly higher than the observed ± 2 % spatial variation (Methods). Thus, it may be assigned to the loss of Pt ions out of the mapped area. To understand if this loss from the mapped area was not due to Pt redistribution to the other parts of the active area caused by an in-plane movement of Pt, 4 $cm^2$ out of the 5 $cm^2$ active area was also mapped (Methods and Supplementary Figure 2b). A similar trend of decrease in average total Pt loading from 558 ± 11 $\mu g.cm^{-2}$ to 498 ± 10 $\mu g.cm^{-2}$ was quantified equating to ~ 10 %. Thus, the heterogeneous degradation resolves the small ~ 3% drop observed in the loss of total average Pt loading between the large 4 $cm^2$ and local inlet area. On the other hand, the total average Pt loading of the outlet was 547 ± 11 $\mu g.cm^{-2}$ and 535 ± 11 $\mu g.cm^{-2}$ before and after AST, respectively. The decrease was negligible compared to the inlet and fell quite close to the observed spatial variation confirming heterogeneous degradation between the inlet and outlet was caused by the modified GDL.

A remarkably high difference in crack development can be observed between inlet and outlet after AST with modified GDL explaining the ~ 13% loss in total average Pt loading and the heterogeneity. The crack formation for the outlet is close to that observed within standard MEA after AST, all of which show minimal change in the total average Pt loading. This further elucidates the role of cracks in through-plane and in-plane transport of Pt ions. **Figure 5c** and **d** show inlet and outlet loading histograms for the modified MEA respectively. The initial unimodal distribution stays the same after the AST for both however, histogram for inlet after the AST shifts left owing to the observed loss in total average Pt loading. The identical location approach allowed successful quantification of evolution of cracks, inlet-outlet degradation heterogeneity and the effect of MEA components on electrocatalyst degradation. Although out of scope for this study, it must be noted that observed loss of Pt loading if via effluent water can be corroborated by ICP-MS of it.

Additional TEM and STEM/EDS analysis of both MEAs after AST at different through-plane locations of the cathode catalyst layer was performed to confirm and complement the observations above. Supplementary Figures 6, 7 and 8 show Pt nanoparticle size growth throughout the cathode catalyst layers of both MEAs along with development of Pt loading hotspots.
Compared to the standard MEA, modified MEA (Supplementary Figure 9) before AST showed identical overpotentials in the kinetic and ohmic regions. Higher cell overpotentials observed in the mass transport region were most likely due to the MPL modification. After AST, cell overpotentials increased more for the modified MEA in all regions driven by relatively high Pt degradation. Cell overpotential increase of 33 mV at 0.8 $A.cm^{-2}$, 54 % loss in mass activity at 0.9 V and 41 % loss in ECSA was observed after AST for the modified MEA. Interestingly, after AST the $H_2$ crossover saw an increase of 16% for the modified MEA indicating increased membrane degradation by combination of cathode catalyst layer and MPL cracks.

**Correlation between Pt nanoparticle size and loading**

**Figure 6a**, **b** and **c** show 300 μm by 300 μm synchrotron μ-X-ray diffraction (μ-XRD) maps of CCM before AST, inlet-after AST and outlet-after AST respectively along with μ-XRF maps of the same location (Methods). No correlation can be observed between Pt nanoparticle size and loading distribution for the CCM before AST. The average Pt nanoparticle size before AST is 3.6 ± 0.5 nm with a Pearson's correlation of – 0.07 between the 2D maps of nanoparticle size and loading (Supplementary Table 1). A Pearson's

correlation of 0 means no linear relationship while a correlation of -1 or +1 indicates complete linear relationship between two maps. The inlet and outlet after AST show a direct linear correlation (positive correlation) between the Pt nanoparticle size and loading with a Pearson's correlation of +0.37 and +0.33, respectively. This means that increase in Pt nanoparticle size is driven by the local increase in Pt loading. The average inlet and outlet Pt nanoparticle size increased to 5.8 ± 1 nm and 6.8 ± 1 nm, respectively. Some local hotspots in the μ-XRD maps show a nanoparticle size increase of almost 8 nm after AST. The synchrotron μ-XRD and μ-XRF maps of the modified MEA (Supplementary Figure 10) also show direct linear correlation with a Pearson's correlation of +0.42 for inlet. More interestingly, the average inlet Pt nanoparticle size increased to 6.8 ± 1 nm even after ~ 13% loss in the total average Pt loading was quantified from the IL-μ-XRF after AST. Thus, coupled with the established correlation above, for a large μm scale region in the cathode catalyst layer undergoing degradation, average Pt nanoparticle size increase and loss in average Pt loading can be mutually inclusive. This finding is extremely important as it provides a blueprint to prevent the depletion of Pt near the membrane-cathode interface in the through-plane direction by developing a hybrid cathode catalyst layer structure with targeted regions of larger Pt nanoparticle size and lower Pt weight % at locations which undergo exacerbated electrocatalyst degradation.

To conclude, commercial CCMs designed for potential HDV applications were subjected to AST simulating HDV lifetime. A simple approach was used to facilitate IL-μ-XRF spectroscopy of MEAs before and after the AST. The results revealed striking in-plane movement of Pt strongly influenced by the initial loading distribution. Increase in the intensity and evolution of local loading hotspots with preferential movement of Pt away from the cathode catalyst layer cracks was observed and successfully quantified. A GDL with cracked MPL was used on the cathode to understand the effect of PEFC components on Pt degradation. The identical location approach exposed heterogeneous degradation between inlet-outlet and allowed quantification of ~ 13% loss in total average Pt loading for the inlet after AST. Synchrotron μ-XRD and μ-XRF experiments showed a direct linear correlation between Pt nanoparticle size and loading, which developed only after AST. The increase in average Pt nanoparticle size to 6.76 nm for modified MEA inlet even after ~ 13% loss in total average Pt loading suggested that nanoparticle size increase and loading loss are mutually inclusive for a cathode catalyst layer area undergoing degradation.

Based on the findings, focused efforts must be put to prevent initial heterogeneous distribution of Pt loading and to avoid development of undesired morphological features in the cathode catalyst layer during the CCM fabrication step. Heterogeneous degradation, in-plane movement of Pt and correlation of nanoparticle size increase with loading loss provide fundamental understanding for development of durable cathode catalyst layers. A hybrid/structured cathode catalyst layer can effectively mitigate significant electrocatalyst degradation. Lastly, current electrocatalyst degradation models must be tuned for each MEA component in use or else the predicted PEFC system lifetime may deviate significantly from the real-world operation.

## Methods

### CCM characterization

CCMs with Pt/C electrocatalyst having anode Pt loading of 50 $\mu g.cm^{-2}$ and cathode Pt loading of 500 $\mu g.cm^{-2}$ were procured. From SEM, the average anode and cathode catalyst layer thicknesses were measured to be ~ 3 μm and ~ 14 μm respectively while the average membrane thickness was measured to be ~ 8 μm (Supplementary Figure 11). Although not required for the scope of this study, it is important to highlight that features like ePTFE reinforcement and radical scavenging additives required for high membrane durability were absent. An average Pt nanoparticle size of 3.8 ± 1.2 nm with unimodal distribution was calculated from TEM before AST (Supplementary Figure 12). The Pt nanoparticles can be observed to be uniformly dispersed over the low surface area carbon support (Supplementary Figure 6a) however elemental mapping does show some local heterogeneity (Supplementary Figure 8).

## MEA preparation and testing hardware

Commercial CCMs were used to prepare two MEAs with 5 $cm^2$ active area. Freudenberg H23C6 was used as both anode and cathode GDL for the first standard MEA. Cracks were introduced in the MPL of only cathode Freudenberg H23C6 GDL to prepare the second modified MEA.

Fuel cell quick connect fixture (qCf) coupled with a cell fixture (cF) from balticFuelCells GmbH (Schwerin, Germany) was used. Two turn 5 $cm^2$ x7 serpentine channel graphite flow field was utilized [41]. The GDL compression in this setup is pneumatically controlled. The manufacturer recommended 1-1.1 MPa pressure of the GDL was achieved by a pneumatic compression pressure of ~ 0.9 bar. This resulted in an optimum 20-22% of GDL compression. Polarization curves and mass activity measurements were performed using 850e fuel cell test system from Scribner Associates (Southern Pines, NC). Cyclic voltammograms (CVs), linear sweep voltammograms (LSVs) and electrochemical impedance spectroscopies (EISs) along with the HDV AST all in nitrogen cathode environment were performed using Interface 5000 potentiostat from Gamry Instruments (Warminster, PA).

## AST and Electrochemical characterization

The ASTs were performed at 80°C cell temperature in 100% RH under atmospheric pressure. **Figure 1a** shows the cell voltage cycle for the HDVAST comprising 0.6 V LPL and 0.9 V of UPL with a dwell time of 3 seconds at each potential. Gas flow rates of 0.2 slpm and 0.2 slpm ($H_2/N_2$) were used for anode and cathode, respectively. During the AST, each MEA was characterized after 0, 10000, 30000, 60000 and 90000 AST cycles.

CVs after cleaning cycles were recorded with a potential scan from 0.1 V to 1.2 V at a scan rate of 100 $mV.s^{-1}$, while LSVs were collected from 0.05 V to 0.8 V at sweep rate of 1 $mV.s^{-1}$ to measure hydrogen crossover. EIS was collected at 0.2 V from 20 kHz to 0.1 Hz with 6 points/decade. All were collected in $H_2/N_2$ environment at 80°C in 100% RH under atmospheric conditions with gas flow rates of 1 slpm/1 slpm on the anode/cathode, respectively. Cell conditioning was performed at 80°C in 100% RH under atmospheric pressure by cycling the voltage between 0.8 V, 0.6 V and 0.3 V (30 seconds each) for 200 cycles in a $H_2$/air environment. Voltage recovery consisted of voltage hold at 0.2 V for 1 hour at 40°C in 150% RH under 150 kPa absolute pressure in a $H_2$/air environment. Polarization curves in $H_2$/air and $H_2$/$O_2$ environments were collected in differential conditions at 80°C in 100% RH under 150 kPa absolute pressure with gas flow rates of 1 slpm/2.5 slpm at anode/cathode, respectively. For air, 4-minute holds from high current density (2 $A.cm^{-2}$) to low current density (0 $A.cm^{-2}$) were performed while for $O_2$ the holds consisted of 3 minutes with increments of 25 mV from 0.75 V to open circuit potential. The data of last minute was averaged and used to plot polarization curves (air) and Tafel plots ($O_2$). A specific order of electrochemical experiments was followed (Supplementary Figure 13b) to get highly reproducible results.

## Modification of MPL

Cracks of ~ 20 μm width were milled into the 35 μm thick free-standing MPL of Freudenberg H23C6 GDL using the ~ 15 μm wide tip of tungsten micro needle. The fabrication was done by hand under an optical microscope (x 20) with a pitch of 1 mm. μ-XCT was performed to confirm the morphology (Supplementary Figure 5). The MPL cracks provided a direct transport pathway between the gas diffusion substrate and the cathode catalyst layer for reactants and products.

## Identical location μ-X-ray fluorescence

A thin 25 μm PTFE template was prepared with alignment markers. Using the cathode flow field as reference, holes were cut out in the template near the inlet and outlet (Supplementary Figure 13a). The

diameter of the holes was kept equal to the diagonal of the 2048 μm by 2048 μm area to be mapped. This ensured automatic alignment of the mapped areas when the template was placed (matching the alignment markers simultaneously) on the MEAs only during μ-XRF mapping before and after the AST. Similarly, a PTFE template with square cut out of 4cm$^2$ area was prepared to facilitate identical location mapping of the larger areas.

*Ex situ* μ-XRF measurements were performed using the XGT-9000 Horiba XRF microscope. A 10 μm capillary was utilized to map an area of 2048 μm by 2048 μm near inlet and outlet with 1024 pixels of detector resolution in both x and y directions giving a final resolution of 2 μm × 2 μm. The larger 20.48 mm × 20.48 mm (~ 4 cm$^2$) area was also mapped using the 10 μm capillary with 1024 pixels of detector resolution in both x and y directions giving a final resolution of 20 μm × 20 μm. The x-ray energy was set to 50 keV. As the x-ray penetrates the full MEA (anode GDL, CCM and cathode GDL), the reflected x-ray signal to the detector includes Pt contribution from both anode and cathode. Thus, the quantified total average Pt loading is the sum of anode and cathode loading. Changes in the total average Pt loading are dominated by the cathode since negligible changes occur in anode (dynamic reference electrode). This allows to reliably obtain information about quantitative changes in the cathode. 2D colormaps were generated in MATLAB using fluorescence images generated by the microscope and the quantified total average Pt loading. The total average Pt loading was quantified for the CCMs using a calibration curve generated from 10 μm capillary maps of calibration samples with known Pt loading. For Pt loading quantification L alpha peak was used. Supplementary Figure 14c shows representative spectrum of a 2048 μm by 2048 μm map.

To further understand variation and to confirm that quantified data reflected true change, the total average Pt loading of each area was reconfirmed by using a larger 1.2 mm capillary at multiple spots (Supplementary Table 2). A variation of ± 2% was observed between the two capillaries. No GDLs were removed from the CCM after AST. The GDLs also made sure that the CCM was completely flat during mapping before and after AST. To make certain that observed in-plane movement of Pt was not due to distortion of the CCM when placed under vacuum, an equilibrium time of ~ 3 hours was provided before any mapping. Lastly, the inlet and outlet were marked on the cathode GDL for further after AST synchrotron experiments.

**μ-X-ray computed tomography**

Ex-situ μ-XCT of standard and modified Freudenberg H23C6 GDL was performed at Beamline 8.3.2 at Advanced Light Source (ALS) at Lawrence Berkeley National Laboratory (LBNL), Berkeley, California using 25 keV energy monochromatic x-rays. 50 μm LuAg:Ce scintillator, 10x lenses and sCMOS PCO.Edge camera were used to achieve an image with 0.65 μm pix$^{-1}$. Exposure time of 200 ms was used to collect 1300 images per scan. Image processing was done using ImageJ.

**Synchrotron μ-X-ray diffraction and fluorescence**

The synchrotron μ-XRD mapping was conducted at Beamline 12.3.2 of the ALS. A monochromatic X-ray beam (10 keV) was focused to 2×5 μm$^2$ by a pair of Kirkpatrick−Baez mirrors. The CCM samples were mounted on a high-resolution x−y scan stage and tilted 20° relative to the incident X-ray beam. 2D X-ray diffraction images were recorded in reflection mode with a two-dimensional Pilatus-1 M detector mounted at 60° to the incoming X-ray, approximately 150 mm from the probe spot. Exposure time at each position was 8 s. Calibrations for distance, center position, and tilt of detector were performed based on ~$Al_2O_3$ powder reference taken at the same geometry. For high resolution mapping of each 0.3 mm × 0.3 mm area of each MEA samples. A 2D scan of 30 × 30 points was performed with a step size of 10 μm. Supplementary Figures 14a and b show representative μ-XRD diffraction pattern and integrated intensity vs 2θ single peaks (Pt 220), respectively. The X-ray diffraction data was processed by XMAS[42]. Change in average Pt

nanoparticle size before and after AST is dominated by the cathode. As negligible nanoparticle size growth occurs at the anode, quantitative information about changes in the cathode can be obtained.

The synchrotron μ-XRF mapping was carried out at the exact identical location using identical raster scan step of the diffraction mapping (start and end point, step size and scan area). The Vortex-EM detector is positioned at an angle to the incoming X-ray beam. The monochromatic X-ray energy was increased to 12 keV for XRF measurements.

**Transmission electron microscopy**

Samples extracted from before AST (Control) MEA, near the inlet of standard MEA, and near the inlet of modified MEA were embedded into an epoxy mixture using an Araldite 6005 epoxy mixture kit (use of approximately 10.7 g Araldite 6005, 7 g Dodecenyl Succinic Anhydride (DDSA) and 0.23 g (DMP-30) 2,4,6, -Tris-(dimethylaminomethyl) phenol) and cured for 16 hours at 68 ºC. A Leica EM Trim2 was used to trim a straight section of the embedded MEA with epoxy on both sides. Ultramicrotomy was done to the block to produce cross-sections of the MEA using a Leica EM UC7 (set to 6 º and a cutting speed of 1 mm $s^{-1}$) and a Diatome diamond knife with an edge length of 2.5 mm and a knife angle of 35 º. Ultrapure deionized water was used in the diamond knife assembly to collect the cross-sections where they were placed onto SPI 3 mm diameter Cu TEM grids (400 mesh slim bar).

Imaging was conducted on a JEOL NEOARM 200CF probe-corrected TEM operated at 200 kV. Elemental mapping was done in STEM mode with EDS using a 70 μm aperture and C-6 spot size setting. Elemental maps were collected at a magnification of 25 kx for ~ 5 minutes using two 100 $mm^2$ JEOL SDD EDS detectors. Post processing of the maps was done using Oxford Instruments AZtec EDS software. Several images acquired at 80 kx, 150 kx, and 500 kx in conventional TEM mode were used to capture through-plane information on the observed degradation phenomena and for nanoparticle size analysis. A 100 μm aperture and a spot size of C-5 was used. Several images were acquired at different locations of the cathode catalyst layer, including areas at the membrane-cathode catalyst layer interface, approximately in the middle of the catalyst layer, and areas at the gas diffusion layer-catalyst layer interface. Nanoparticle size analysis of before AST (Control) sample was done manually on images taken at 500 kx using imageJ's freehand tool to measure the area of the selected nanoparticle's region. It should be noted that measurements were only made to nanoparticles that could be distinguished; agglomerates or overlapping nanoparticles were not analyzed. The equivalent diameter was back calculated assuming a circular particle shape. The measured equivalent diameters were then analyzed using MATLAB's 'Distribution Fitter' application (MATLAB 2022a). The bin size was preset to 0.5 nm width and a probability distribution function (PDF) analysis was used to fit a lognormal distribution to the measured equivalent diameters. To better estimate the localized nanoparticle size, a minimum of 3 images and 200 nanoparticles were used in general as a guideline at each region. An iterative approach was used at each region until the mean value of the nanoparticle size did not change significantly. A total of 1241 nanoparticles were measured for the before AST (Control) MEA. An overall PSD combining the measurements of all three regions is reported.

**Scanning electron microscopy**

MEA samples were potted in epoxy to prepare cross sections. The MEA samples were first placed in between and supported by stainless steel foil in the epoxy. The samples were then polished using a Buehler EcoMet 30 polishing paper gradually progressing from grit number 320 to 1200. Images of the polished cross-section were recorded using a scanning electron microscope (JEOL SEM 7200F) in secondary electron mode with 5-15kV accelerating voltage.

**Data availability**

The authors declare that the data supporting the findings of this study are available within the paper and its Supplementary Information. Source data are provided with this paper.


## Acknowledgements

XRF was performed at HIMAC2 Analytic Laboratory, a user facility operated by the Horiba Institute for Mobility and Connectivity, University of California Irvine. The Advanced Light Source is supported by the Director, Office of Science, Office of Basic Energy Sciences, of the U.S. Department of Energy under Contract No. DE-AC02-05CH11231. We thank Dr. Dula Parkinson for the beamline support.


## Author contributions

K.K. and A.Z. were chiefly responsible for most of the experiments. L.C. and N.T. performed combined XRD and XRF experiments at the synchrotron. M.C. and S.P. performed microscopy experiments. P.A., L.C, J.B., C.J. and I.Z. helped with data interpretation and did conception of the study. K.K. produced the first manuscript draft and all the authors edited it. L.C., C.J., P.A. and I.Z. obtained funding support and oversaw the study.

## Competing Interests

The authors declare no competing interests.

## Figure Captions (for main text figures)

**Figure 1| Single cell voltage cycle of the accelerated stress test (AST) and ECSA loss pathways. a**, Square cell voltage cycle consisting of 0.6 V lower potential limit (LPL) and 0.9 V upper potential limit (UPL) with a hold time of 3 seconds each. To simulate heavy-duty vehicle lifetime equivalent to ≥ 25,000 hours, the square cell voltage cycle is repeated 90,000 times. **b**, Schematic of three ECSA loss pathways caused by dissolution of $Pt^{X+}$ ions from Pt nanoparticles.

**Figure 2| Electrochemical characterization after 0, 10k, 30k, 60k and 90k AST cycles. a**, Polarization curves with high frequency resistance (HFR) collected at 80°C in 100% RH under 150 kPa of absolute pressure in $H_2$-air differential environment. **b**, ECSA calculated from CVs collected at 80°C in 100% RH under 100 kPa of absolute pressure in $H_2$-$N_2$ environment. **c**, Tafel plots generated from $H_2$-$O_2$ differential environment data collected at 80°C in 100% RH under 150 kPa of absolute pressure. (Inset) Mass activity at 0.9 V calculated from the corresponding Tafel plots.

**Figure 3| Identical location-μ-XRF spectroscopy of the standard membrane electrode assembly. a**, **b** In-plane Pt loading maps of inlet (**a**) and outlet (**b**) with regions marked to establish identical location before and after the accelerated stress test (AST). **c**, **d** Corresponding histograms of the inlet and outlet respectively showing the unchanged unimodal Pt loading distribution before and after the AST. Scale bars, 500 μm.

**Figure 4| In-plane movement of Pt. a**, **b** Local ~ 400 μm × 400 μm areas before and after the accelerated stress test (AST) from inlet (**a**) and outlet (**b**) Identical location-μ-XRF maps of the standard membrane electrode assembly. Marked regions highlight evolution of local loading hotspots and preferential movement of Pt away from cracks after the AST. Scale bar, 100 μm.

**Figure 5| Identical location-μ-XRF spectroscopy of the modified membrane electrode assembly. a**, **b** In-plane Pt loading maps of inlet (**a**) and outlet (**b**) before and after the accelerated stress test (AST). **c**, **d** Corresponding Pt loading distribution histograms of the inlet and outlet respectively. Unimodal distribution was unchanged before and after the AST however a loss in inlet average total Pt loading was observed. Scale bars, 500 μm.

**Figure 6| Synchrotron μ-XRD and μ-XRF spectroscopy of standard membrane electrode assembly (MEA) identical locations after accelerated stress test (AST). a**, Before AST 300 μm × 300 μm maps showing no correlation between Pt nanoparticle size and loading distribution. **b**, **c** Inlet and outlet of the standard MEA respectively showing a strong linear correlation between Pt nanoparticle size and loading distribution after AST. Scale bar 50 μm.

## References


1. D. Cook, UCS, Engines for Change. (2015)
2. EPA 430-R-22-003 Inventory of U.S. Greenhouse Gas Emissions and Sinks, 1990 to 2020. (2020).
3. Papageorgopoulos, D. Fuel Cell R&D Overview. *2019 Annu. Merit Rev. Peer Eval. Meet.* 33 (2019).
4. Cherevko, S., Kulyk, N. & Mayrhofer, K. J. J. Durability of platinum-based fuel cell electrocatalysts: Dissolution of bulk and nanoscale platinum. *Nano Energy* **29**, 275–298 (2016).
5. Meier, J. C. *et al.* Design criteria for stable Pt/C fuel cell catalysts. *Beilstein J. Nanotechnol.* **5**, 44–67 (2014).
6. Borup, R. L. *et al.* Recent Developments in Catalyst-Related PEM Fuel Cell Durability. *Curr. Opin. Electrochem.* (2020) doi:10.1016/j.coelec.2020.02.007.
7. Borup, R. *et al.* Scientific aspects of polymer electrolyte fuel cell durability and degradation. *Chem. Rev.* **107**, 3904–3951 (2007).
8. Yu, H. *et al.* Tracking Nanoparticle Degradation across. (2022) doi:10.1021/acsnano.2c02307.
9. Lee, C. *et al.* Towards a Comprehensive Understanding of Cation Effects in Proton Exchange Membrane Fuel Cells. *ACS Appl. Mater. Interfaces* (2022) doi:10.1021/acsami.2c07085.
10. Annual Energy Outlook 2019 with projections to 2050. **44**, 1–64 (2019).
11. Perez-Alonso, F. J. *et al.* Identical locations transmission electron microscopy study of Pt/C electrocatalyst degradation during oxygen reduction reaction. *J. Power Sources* **196**, 6085–6091 (2011).
12. Gilbert, J. A. *et al.* Pt catalyst degradation in aqueous and fuel cell environments studied via in-operando anomalous small-angle X-ray acattering. *Electrochim. Acta* **173**, 223–234 (2015).
13. Stariha, S. *et al.* Recent Advances in Catalyst Accelerated Stress Tests for Polymer Electrolyte Membrane Fuel Cells. *J. Electrochem. Soc.* **165**, F492–F501 (2018).
14. Lazaridis, T., Stühmeier, B. M., Gasteiger, H. A. & El-Sayed, H. A. Capabilities and limitations of rotating disk electrodes versus membrane electrode assemblies in the investigation of electrocatalysts. *Nat. Catal.* **5**, 363–373 (2022).
15. Khedekar, K. *et al.* Probing Heterogeneous Degradation of Catalyst in PEM Fuel Cells under Realistic Automotive Conditions with Multi-Modal Techniques. *Adv. Energy Mater.* **11**, (2021).
16. Khedekar, K. *et al.* Effect of Commercial Gas Diffusion Layers on Catalyst Durability of Polymer Electrolyte Fuel Cells in Varied Cathode Gas Environment. *Small.***18**, (2022).
17. Yu, H. *et al.* Recreating Fuel Cell Catalyst Degradation in Aqueous Environments for Identical-Location Scanning Transmission Electron Microscopy Studies. *ACS Appl. Mater. Interfaces* (2021) doi:10.1021/acsami.1c23281.
18. Cheng, L. *et al.* Mapping of Heterogeneous Catalyst Degradation in Polymer Electrolyte Fuel Cells. *Adv. Energy Mater.* **10**, (2020).
19. Martens, I. *et al.* Imaging Heterogeneous Electrocatalyst Stability and Decoupling Degradation

Mechanisms in Operating Hydrogen Fuel Cells. *ACS Energy Lett.* **6**, 2742–2749 (2021).

20. Greenhouse Gas Emissions and Fuel Efficiency Standards for Medium- and Heavy-Duty Engines and Vehicles—Phase 2 US Environmental Protection Agency, (2016) https://www.govinfo.gov/content/pkg/FR-2016-10-25/ pdf/2016-21203.pdf

21. Geyer, H. K. & Ahluwalia, R. K. GCtool for Fuel Cell Systems Design and Analysis: User Documentation. (1998).

22. Cullen, D. A. *et al.* New roads and challenges for fuel cells in heavy-duty transportation. *Nat. Energy* **6**, 462–474 (2021).

23. Inaba, M. *et al.* The Oxygen Reduction Reaction on Pt: Why Particle Size and Interparticle Distance Matter. *ACS Catal.* 2021, 11, 7584−7594.

24. Schröder, J. *et al.* Investigating the Particle Growth in Bimodal Pt/C Catalysts by In-Situ Small Angle X-ray Scattering: Challenges in the Evaluation of Stress Test Protocol-Dependent Degradation Mechanisms. *J. Electrochem. Soc.* 2022 **169** 104504.

25. Schröder, J. *et al.* Tracking the Catalyst Layer Depth-Dependent Electrochemical Degradation of a Bimodal Pt/C Fuel Cell Catalyst: A Combined Operando Small- and Wide-Angle X-ray Scattering Study. *ACS Catal.* 2022, 12, 2077−2085.

26. Larbi, B., Alimi, W., Chouikh, R. & Guizani, A. Effect of porosity and pressure on the PEM fuel cell performance. *Int. J. Hydrogen Energy* **38**, 8542–8549 (2013).

27. Zhang, J., Litteer, B. A., Gu, W., Liu, H. & Gasteiger, H. A. Effect of Hydrogen and Oxygen Partial Pressure on Pt Precipitation within the Membrane of PEMFCs. *J. Electrochem. Soc.* **154**, B1006 (2007).

28. Myers, D. J., Wang, X., Smith, M. C. & More, K. L. Potentiostatic and Potential Cycling Dissolution of Polycrystalline Platinum and Platinum Nano-Particle Fuel Cell Catalysts. *J. Electrochem. Soc.* **165**, F3178–F3190 (2018).

29. Kneer, A., Wagner, N., Sadeler, C., Scherzer, A.-C. & Gerteisen, D. Effect of Dwell Time and Scan Rate during Voltage Cycling on Catalyst Degradation in PEM Fuel Cells. *J. Electrochem. Soc.* **165**, F805–F812 (2018).

30. Zhang, H. *et al.* The Impact of Potential Cycling on PEMFC Durability. *J. Electrochem. Soc.* **160**, F840–F847 (2013).

31. Gatalo, M. *et al.* Importance of Chemical Activation and the Effect of Low Operation Voltage on the Performance of Pt-Alloy Fuel Cell Electrocatalysts. *ACS Appl. Energy Mater.* 2022, 5, 8862.

32. Fuel Cells 2016 Multi-Year Research, Development, and Demonstration Plan (2016 https://energy.gov/sites/prod/files/2016/10/f33/fcto_myrdd_fuel_cells.pdf).

33. Kongkanand, A. & Mathias, M. F. The Priority and Challenge of High-Power Performance of Low-Platinum Proton-Exchange Membrane Fuel Cells. *J. Phys. Chem. Lett.* **7**, 1127–1137 (2016).

34. Harzer, G. *et al.* Cathode Loading Impact on Voltage Cycling Induced PEMFC Degradation: A Voltage Loss Analysis. *J. Electrochem. Soc.* **165** (6) F3118-F3131 (2018).

35. Kabir, S. *et al.* Elucidating the Dynamic Nature of Fuel Cell Electrodes as a Function of Conditioning: An ex Situ Material Characterization and in Situ Electrochemical Diagnostic study.

*ACS Appl. Mater. Interfaces* 2019, 11, 45016-45030

36. Gasteiger, H. A., Panels, J. E. & Yan, S. G. Dependence of PEM fuel cell performance on catalyst loading. *J. Power Sources* **127**, 162–171 (2004).

37. Wang, M. *et al.* Impact of Catalyst Ink Dispersing Methodology on Fuel Cell Performance Using in-Situ X-ray Scattering. (2019) doi:10.1021/acsaem.9b01037.

38. Cetinbas, F. C., Ahluwalia, R. K., Shum, A. D. & Zenyuk, I. V. Direct Simulations of Pore-Scale Water Transport through Diffusion Media. *J. Electrochem. Soc.* **166**, F3001–F3008 (2019).

39. Tan, Y. *et al.* Pt–Co/C Cathode Catalyst Degradation in a Polymer Electrolyte Fuel Cell Investigated by an Infographic Approach Combining Three-Dimensional Spectroimaging and Unsupervised Learning. *J. Phys. Chem. C* 2019, 123, 31, 18844–18853.

40. Matsui, H. et al. Operando 3D Visualization of Migration and Degradation of a Platinum Cathode Catalyst in a Polymer Electrolyte Fuel Cell. *Angew.Chem.Int.Ed.* 2017,56,9371 –9375.

41. Simon, C., Hasché, F. & Gasteiger, H. A. Influence of the Gas Diffusion Layer Compression on the Oxygen Transport in PEM Fuel Cells at High Water Saturation Levels. *J. Electrochem. Soc.* **164**, F591–F599 (2017).

42. Barabash, Rozaliya, and Gene Ice. Strain and Dislocation Gradients from Diffraction: Spatially resolved Local Structure and Defects (2014).

**a**

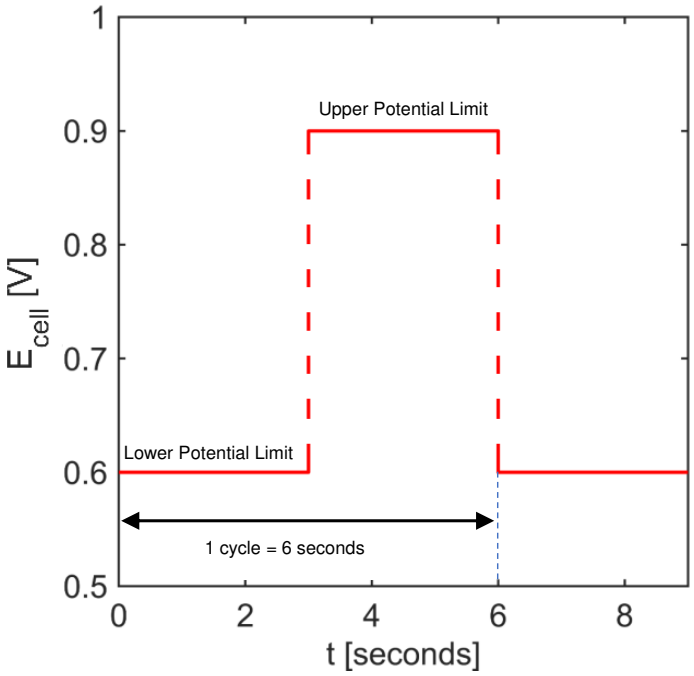
Upper Potential Limit
Lower Potential Limit
1 cycle = 6 seconds
E_cell [V]
t [seconds]
1
0.9
0.8
0.7
0.6
0.5
0
2
4
6
8

**b**

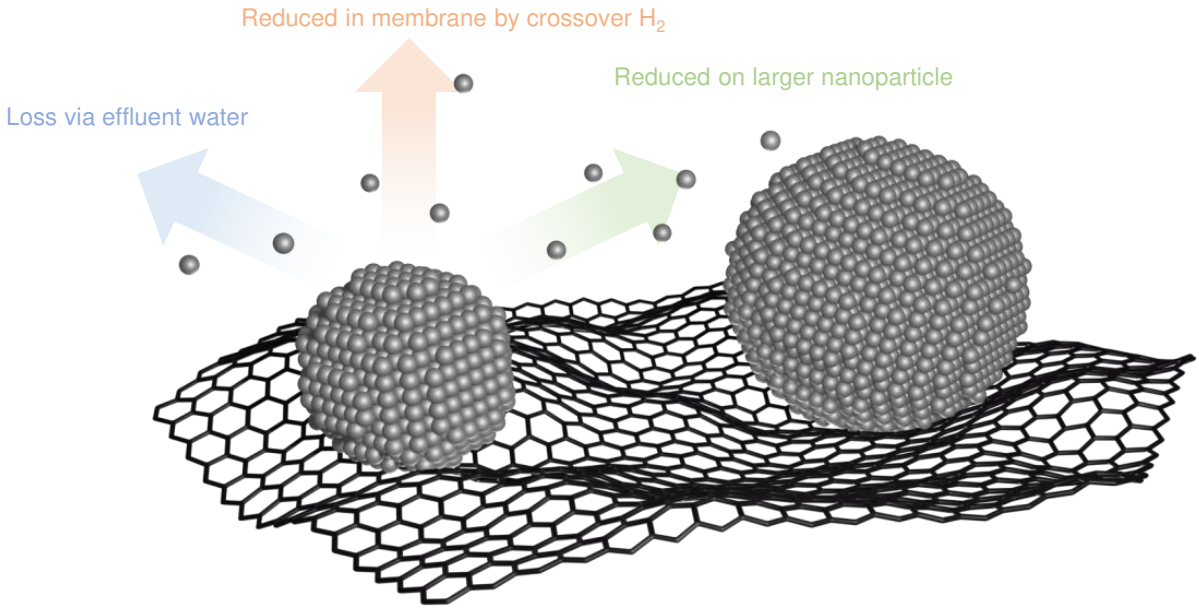
Reduced in membrane by crossover H2
Reduced on larger nanoparticle
Loss via effluent water

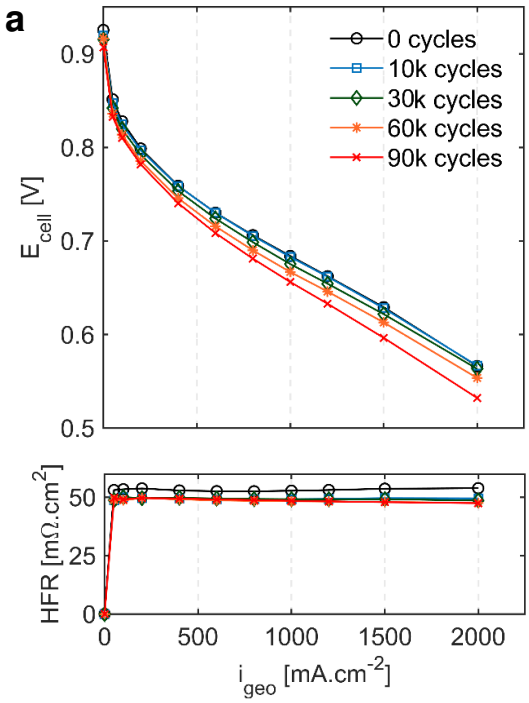
a
0 cycles
10k cycles
30k cycles
60k cycles
90k cycles
E_cell [V]
HFR [mΩ.cm²]
i_geo [mA.cm⁻²]

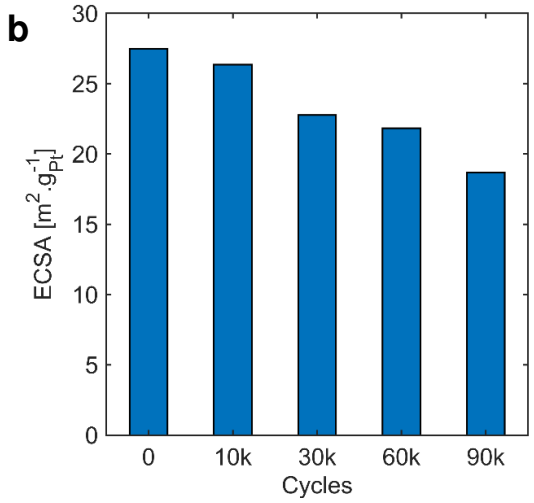
b
ECSA [m².g_Pt⁻¹]
Cycles

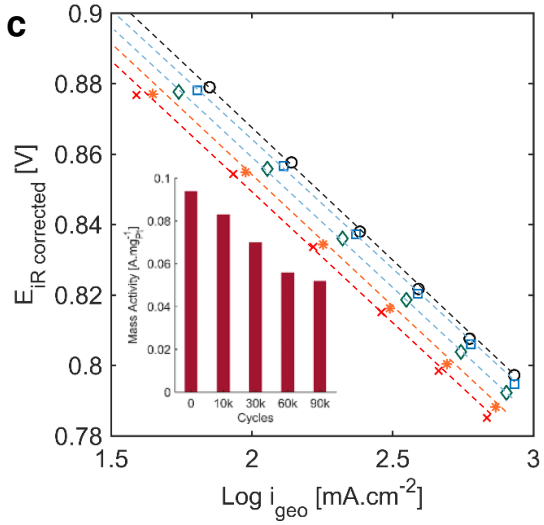
c
E_iR corrected [V]
Log i_geo [mA.cm⁻²]
Mass Activity [A.mg_Pt⁻¹]
Cycles

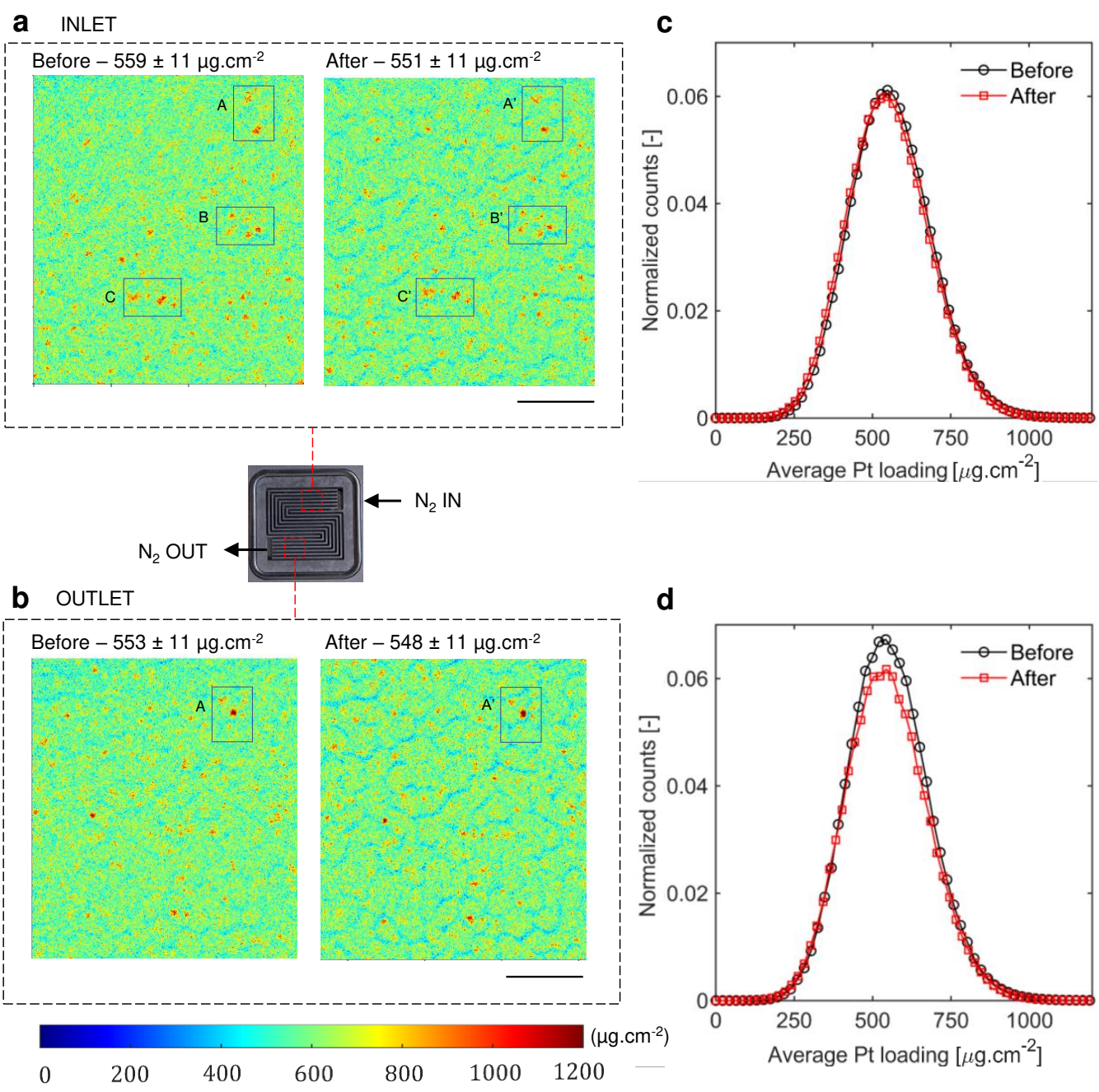
a
INLET
Before – 559 ± 11 µg.cm-2
After – 551 ± 11 µg.cm-2
A
B
C
A'
B'
C'
N2 IN
N2 OUT
b
OUTLET
Before – 553 ± 11 µg.cm-2
After – 548 ± 11 µg.cm-2
A
A'
(µg.cm-2)
0
200
400
600
800
1000
1200
c
Before
After
Normalized counts [-]
0.06
0.04
0.02
0
0
250
500
750
1000
Average Pt loading [µg.cm-2]
d
Before
After
Normalized counts [-]
0.06
0.04
0.02
0
0
250
500
750
1000
Average Pt loading [µg.cm-2]

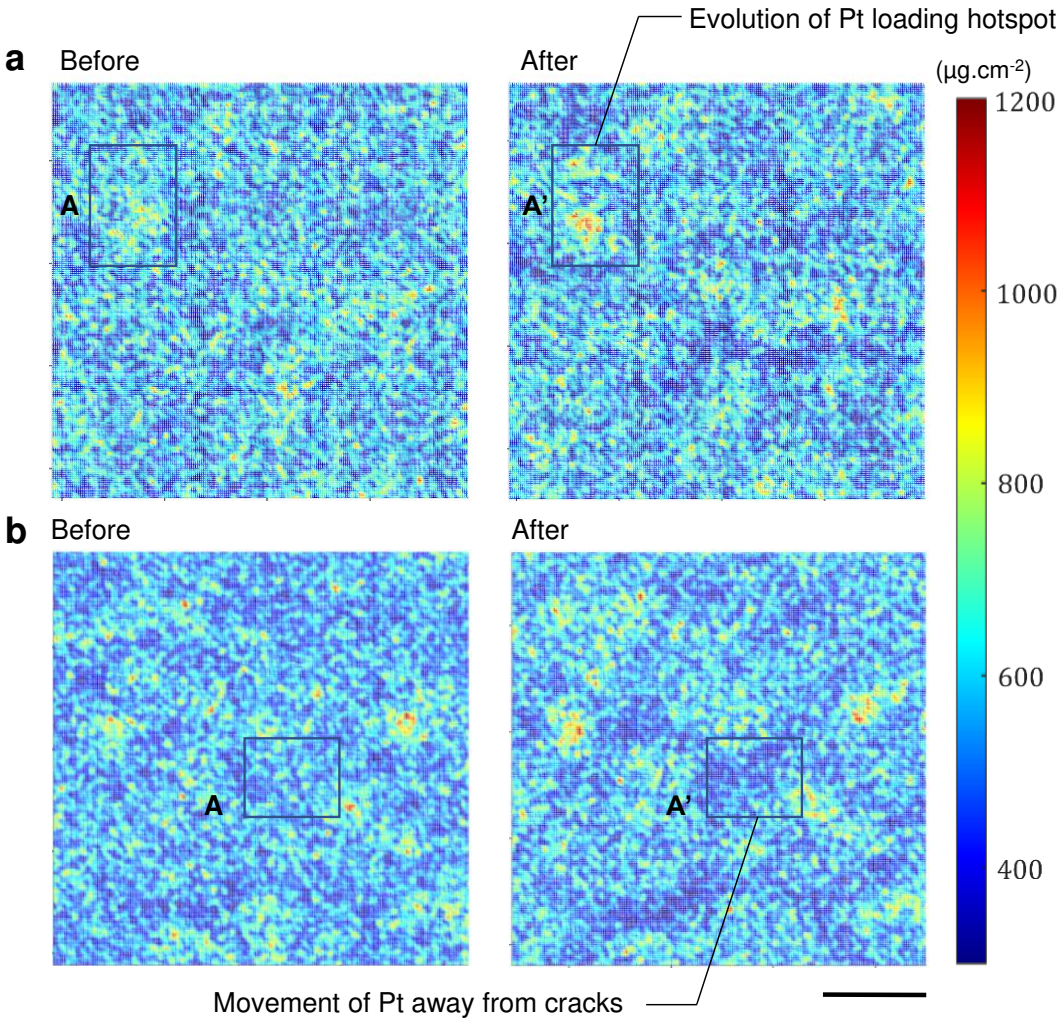
a
Before
After
Evolution of Pt loading hotspot
(µg.cm-2)
1200
1000
800
600
400
A
A'
b
Before
After
A
A'
Movement of Pt away from cracks

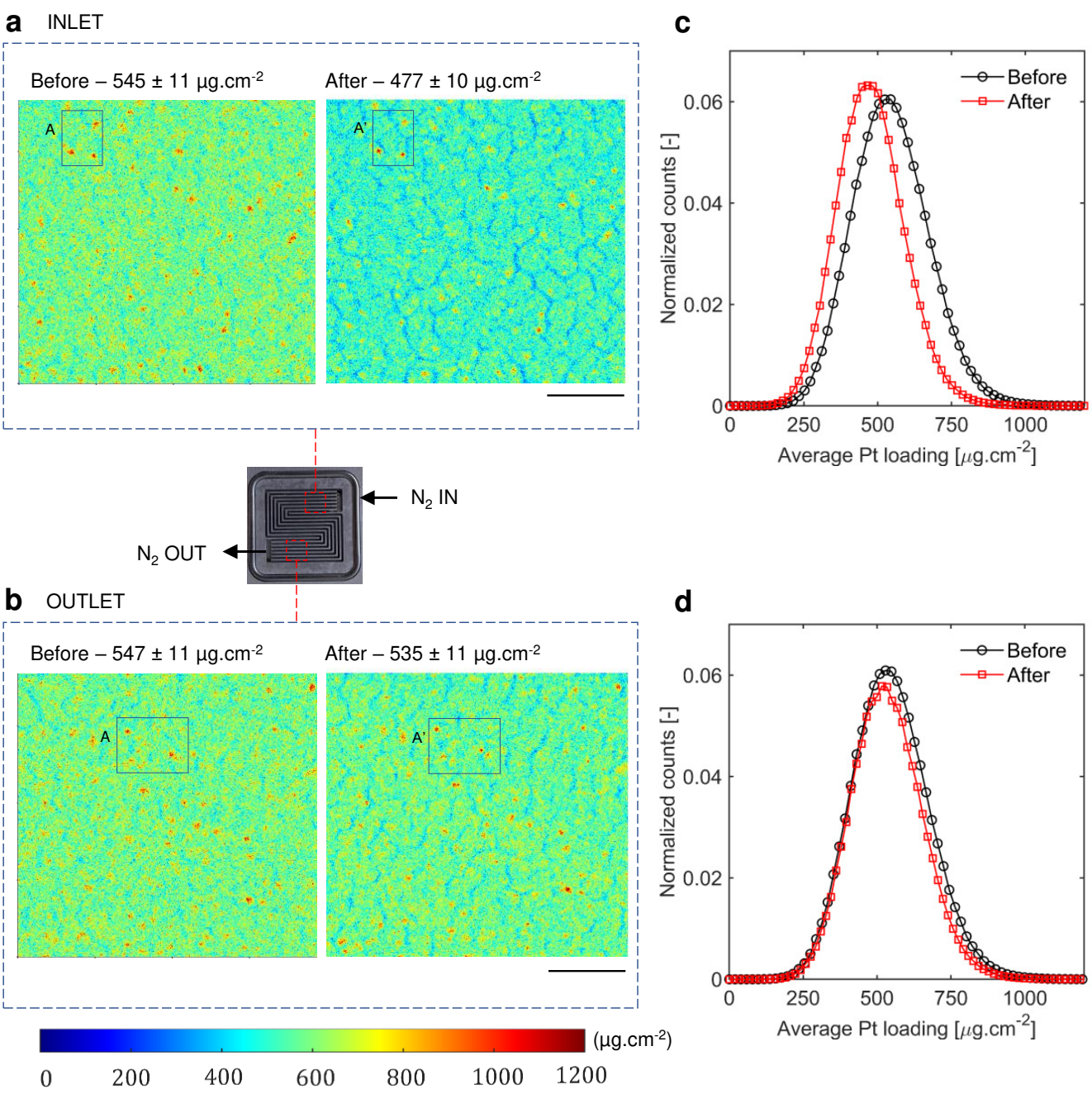
a INLET
Before – 545 ± 11 µg.cm-2
After – 477 ± 10 µg.cm-2
A
A'
N2 IN
N2 OUT
b OUTLET
Before – 547 ± 11 µg.cm-2
After – 535 ± 11 µg.cm-2
A
A'
(µg.cm-2)
0 200 400 600 800 1000 1200
c
Before
After
Normalized counts [-]
0 0.02 0.04 0.06
0 250 500 750 1000
Average Pt loading [µg.cm-2]
d
Before
After
Normalized counts [-]
0 0.02 0.04 0.06
0 250 500 750 1000
Average Pt loading [µg.cm-2]

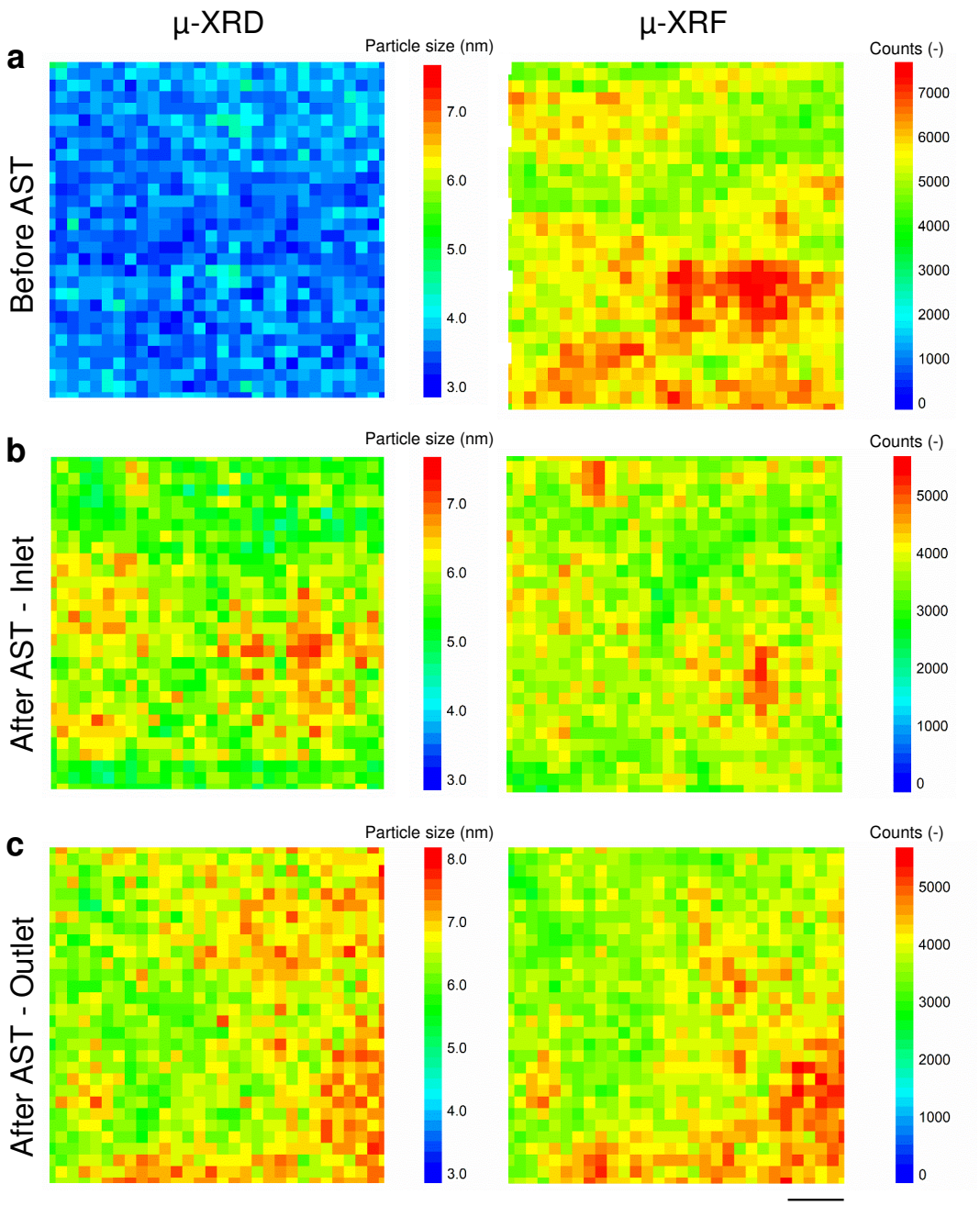
μ-XRD
μ-XRF
a
Before AST
Particle size (nm)
7.0
6.0
5.0
4.0
3.0
Counts (-)
7000
6000
5000
4000
3000
2000
1000
0
b
After AST - Inlet
Particle size (nm)
7.0
6.0
5.0
4.0
3.0
Counts (-)
5000
4000
3000
2000
1000
0
c
After AST - Outlet
Particle size (nm)
8.0
7.0
6.0
5.0
4.0
3.0
Counts (-)
5000
4000
3000
2000
1000
0

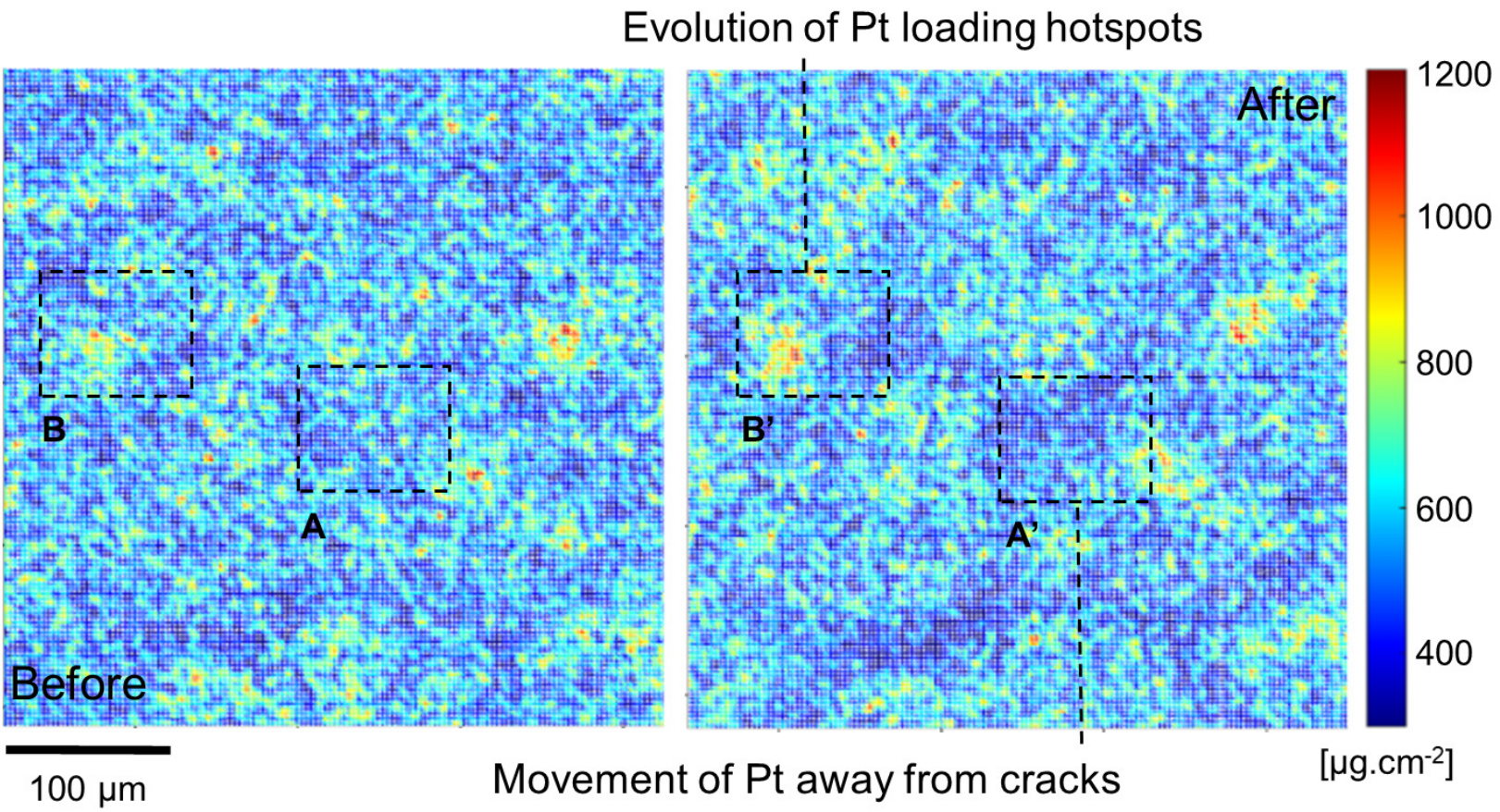
Evolution of Pt loading hotspots
After
Before
B
A
B'
A'
1200
1000
800
600
400
[µg.cm-2]
100 µm
Movement of Pt away from cracks